SIMULATION OF A SOLID PROPELLANT SUBSCALE MOTOR WITH A 3D PROTRUDING INHIBITOR

E. Radenac, G. Casalis, Y. Fabignon, M. Prévost
ONERA

ABSTRACT

Most segmented solid rocket motors exhibit pressure oscillations due to aeroacoustic instabilities involving vortex sheddings. Inhibitors are often involved in these instabilities. In addition, an intrinsic hydrodynamic instability of flows induced by wall injection sometimes leads to a parietal vortex shedding that can have a major influence on pressure oscillations. The present paper intends to understand better how pressure oscillations are modified when a 3D protruding inhibitor is used instead of a usual ring-shaped inhibitor. A reduced-scale experiment involving such an inhibitor showed that pressure oscillations are damped but an instablity bump remains with quite disorganized frequency changes. Moreover, pressure oscillation levels, although still low, are enhanced near the frequency of the second longitudinal acoustic mode.

To understand the underlying physics, a 3D simulation was performed with the ONERA in-house code, CEDRE, at the time of largest oscillation level. This work mainly focuses on this numerical study. After a mesh convergence, it appeared that an hexaedral mesh with sufficiently large number of cells (about 4.3 million cells) was necessary to overcome numerical dissipation and obtain a spectral behaviour close to the experimental results, even if instability levels are still lower than those experimentally found. Numerical schemes also had to be chosen carefully. Moreover, turbulence can be suspected to play a role in the dissipation of the vortices and it was modeled by a MILES approach.

Post-processing of simulations gives a noisy pressure signal and frequency peaks in particular on both first and second longitudinal acoustic modes. A 3D interaction between the obstacle vortex shedding due to the 3D inhibitor and the parietal vortex shedding occurs, as well as a complex interaction between vortices stemming from different neighbouring locations of the inhibitor. All these interactions lead to less coherent large vortices than with a ring-shaped inhibitor and it may be part of the explanation of the role played by the 3D inhibitor in damping instabilities.

INTRODUCTION

Instabilities in solid rocket motors is a critical issue that is likely to involve thrust oscillations and consequently dynamic loads on the payload.

Pressure oscillations in large segmented solid rocket motors are mainly due to the coupling of the chamber acoustics with vortex sheddings caused by hydrodynamic instabilities. These vortex sheddings can be caused either by the Taylor flow intrinsic instability (parietal vortex shedding, PVS) or by a shear layer instability in the wake of protruding inhibitors for instance (obstacle vortex sheddings, OVS). So, these inhibitors are often involved in the coupling of vortex sheddings with acoustics, when the frequency of the hydrodynamic instability is close to the frequency of an acoustic mode.

An idea to reduce (through a passive control approach) the coupling between the vortex shedding and the acoustics was to give the inhibitor a 3D shape (figure 1). This shape is intended to make large vortices less coherent, thanks to a non-axisymmetric structure. It was tested twice in ARTA 03 bench firings [1], and a preliminary reduced scale experiment (1/15th LP6) had also been carried out at the ONERA. In the LP6 experiment, the inhibitor was made of metal, so that no deformation occurs and the shape is known precisely. Moreover reducing the scale of flexible inhibitors is not straightforward. It must be noticed that the shape of the rigid inhibitor is representative of the mean deformation of the real inhibitor during the firing and that similar experiments with a ring-shaped inhibitor exist [2]. Compared to these references that exhibit strong oscillations, the motor equipped with a 3D inhibitor is stable.

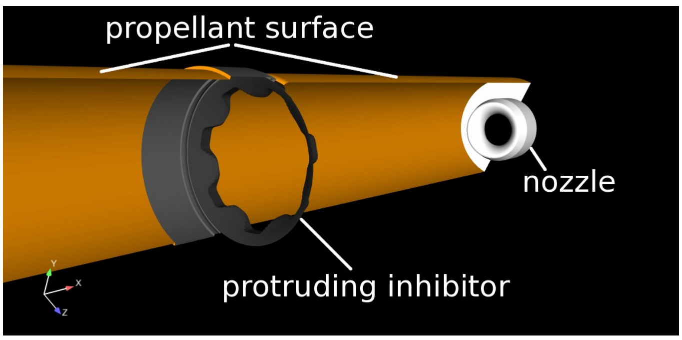

Illustration 1: 3D shape of the protruding inhibitor.

SUBSCALE EXPERIMENT MAIN RESULTS

The subscale LP6 experiment showed that pressure oscillations are strongly modified by the introduction of a 3D shaped inhibitor. The levels are clearly lower than with a classical ring-shaped inhibitor. But an instability bump remains (from time 8 to 10s, in figure 2) with quite disorganized frequency changes. An analysis with the HRogram method shows (in figure 3) that oscillation frequencies are mainly distributed around first, second and third longitudinal acoustic modes (1L, 2L and 3L) but it does not appear that a mode is strongly locked on. The HRogram method [3] [4] allows to compute the time-dependent amplitude and frequencies of a definite number of modes (11 modes were computed here).

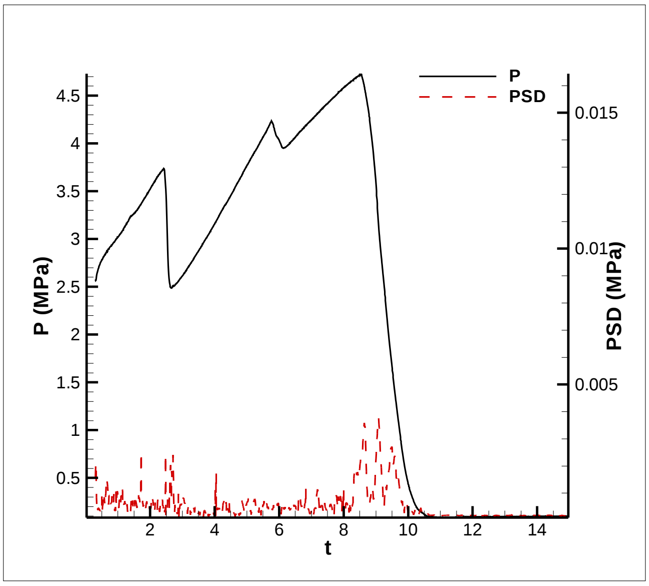

Illustration 2: Time-dependent mean pressure and power spectral density (PSD) at the head-end of the subscale LP6 experiment.

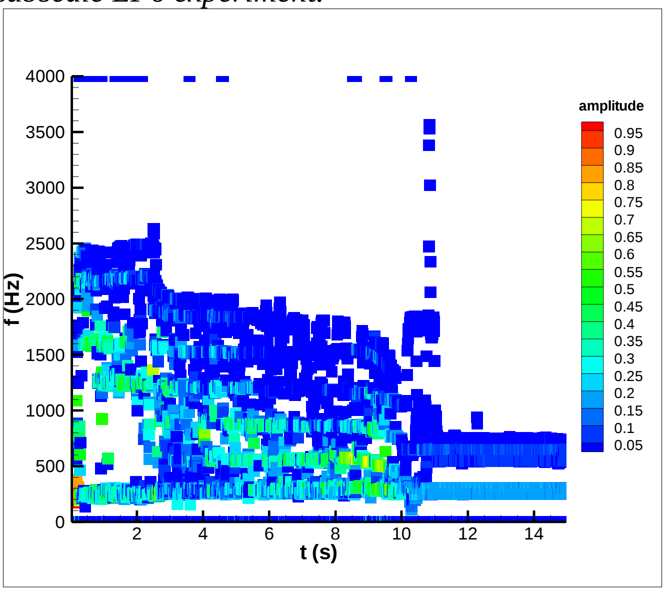

Illustration 3: HRogram analysis of pressure at the head-end, LP6 experiment.

Moreover, during the instability bump, pressure oscillation levels are still low but it involves mainly the excitation of the second longitudinal acoustic mode.

PURPOSE OF THE COMPUTATIONS

Numerical simulations of the 1/15th scale experiment were performed at the time of largest oscillation level (8.6s) in order to provide a better understanding of the results of the firing and of the phenomena occuring in the motor (OVS and PVS interaction, enhancement of turbulence). A fixed geometry could be used because aerodynamic and acoustic time scales are far smaller than burnback time scale.

Numerical computations using several grids were actually necessary to obtain significant results (table 1). This paper will focus on the simulation using the largest grid (M4). But the results obtained with other grids need to be sumed up.

For the sake of simplicity, a first 3D simulation was performed using a 2,032,870 cell unstructured mesh (M0). This computation happened to be stable. It was attributed to a too large numerical dissipation caused by the unstructured grid.

That is why a new set of 3D computations was defined, using structured (O-grid) meshes of increasing size (M1, M2, M3 and M4), such grids allowing less numerical dissipation.

Moreover, it is interesting to notice that two 2D computations were performed to assess the consequence of an inhibitor of similar shape as the 3D inhibitor but with minimal (M5, small section reduction) or maximal (M6, large section reduction) height (figure 2). Unstructured meshes were used for these 2D simulations. This approach provides pressure fluctuations, but more details will be given when comparing M4, M5 and M6 grid results.

Name	Characteristics	Number of elements
M0	Unstructured, 3D	2,032,870
M1	Structured, 3D	282,591
M2	Structured, 3D	807,270
M3	Structured, 3D	2,260,728
M4	Structured, 3D	4,288,000
M5	Untructured, 2D	61,965
M6	Untructured, 2D	63,346

Table 1 : Summary of the different grids.

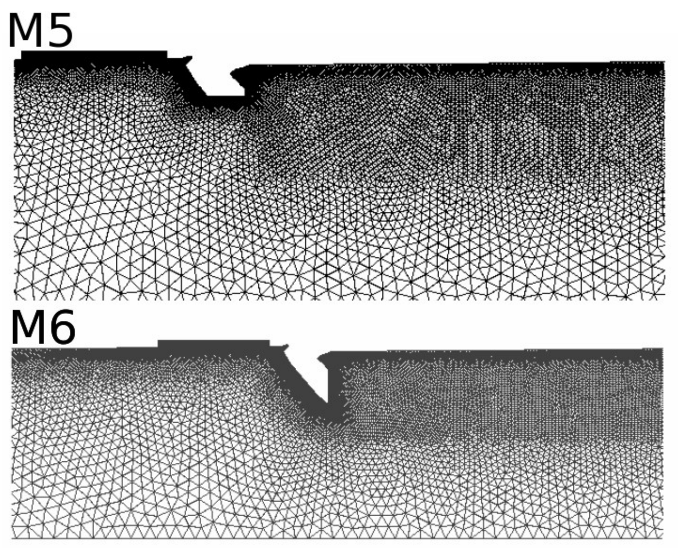

Illustration 4: M5 and M6 grids : minimal and maximal length of the 3D inhibitor.

NUMERICAL MODEL

3D computations were performed with CEDRE, the Finite-Volume CFD code from ONERA. A single-phase approach was used (with the fluid solver, CHARME), because the propellant used in the subscale experiment does not contain aluminum particles. The Navier-Stokes equations were solved using second-order numerical schemes.

The combustion of the propellant is simply modeled by an injection boundary condition at constant flow-rate q_p and temperature T_p.

Turbulence is treated with a MILES approach (the subgrid model is given by the numerical scheme diffusivity).

The spatial integration is made with a Roe scheme. Second-order is achieved with a MUSCL scheme (with a Van Leer slope limiter). The temporal scheme is an explicit two-step Runge-Kutta scheme, second-order accurate.

Inert surfaces are treated as isothermal or adiabatic walls. In the first case, the surface temperature of the protruding inhibitor is T_{in}, the temperature of the head-end, aft-end and cylinder walls is T_{he}.

The molar mass M, the specific heat capacity at constant pressure C_p, the dynamic viscosity μ, and the Prandtl number Pr defining the fluid properties are given in table 2, as well as the propellant burning rate q_p and temperature T_p and the surface temperatures T_{in} and T_{he}.

The integration was achieved with a Courant-Friedrichs-Lewy number around CFL=0.3. For a satisfactory frequential accuracy, a large number of iterations is often necessary for pressure oscillation characterization. For grid M4, 2.5 million iterations were run.

M (*kg/mol*)	24.394 10^{-3}
C_p (*J/K/kg*)	2153.8
μ (*kg/m/s*)	8.07 10^{-5}
Pr	0.45
q_p (*kg/s/m²*)	12.025
T_p (K)	2688
T_{in} (K)	500
T_{he} (K)	2500

Table 2 : Physical parameters for the computations.

NUMERICAL RESULTS

Numerical simulations with all three grids M1, M2 and M3 were stable. Figure 5 shows the pressure at the head-end with grid M3 for instance. It can be noticed that removing the slope limiter gave rise to a weakly oscillating pressure signal with grid M3. This approach was intended to destabilize slightly the numerical scheme to favour and sustain the oscillations. The signal is modulated but the main frequency is around 300 Hz, that is 1L acoustic mode. The 2L acoustic mode is weak. It is not satisfactory in comparison to the experiment. Moreover, it is not clear if the modulation is due to physical or numerical reasons.

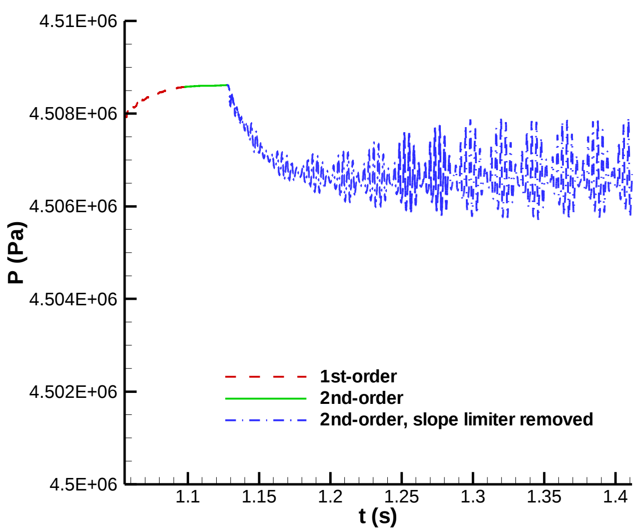

Illustration 5: Pressure at the head-end, grid M3. First-order time integration, second-order time integration with and then without a slope limiter.

Using a stable integration scheme, pressure oscillations were obtained only with the larger mesh, M4. The instability level at the head-end is 318Pa (up to 425Pa, if the Van Leer slope limiter is replaced by the less diffusive Superbee slope limiter), which is seven times less than experimentally found, but not negligible. The pressure signal at the head-end is shown in figure 6. Moreover, it is interesting to notice that the signal is rather noisy and two dominant frequencies are identified near the first two longitudinal acoustic modes (as shown in figure 7 at the head-end).

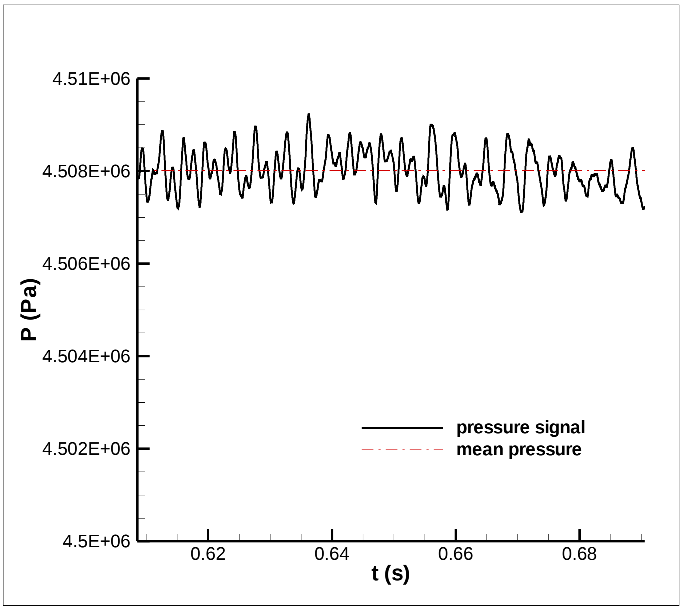

Illustration 6: Pressure at the head-end, grid M4.

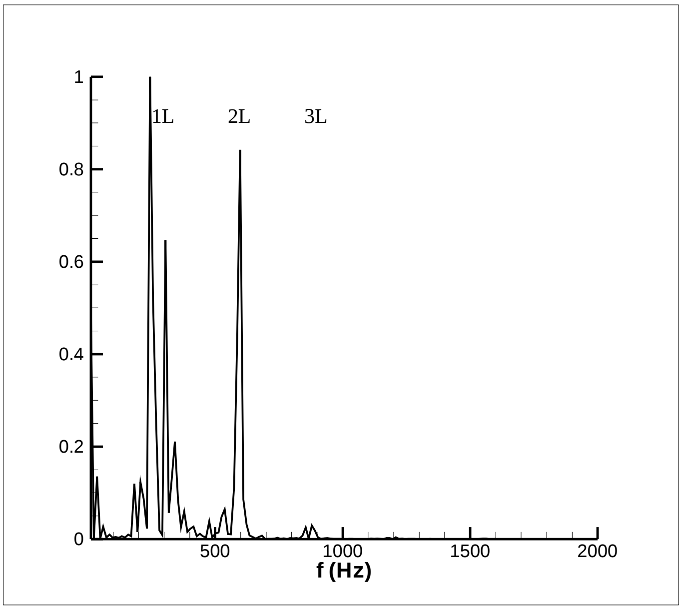

Illustration 7: Power spectral density, pressure at the head-end, 2^{13}points, Δf=12Hz, $\Delta t=10^{-5}$s. Grid M4.

A vorticity field downstream of the inhibitor is displayed in figure 8. It can be compared to the vorticity field given by ring-shaped protruding inhibitors (computations with grids M5 and M6, figure 9). The approaches used for the computations are different but at first sight, the behaviour appears to be quite similar to M5 in the wake of small inhibitor height (at the bottom of figure 8) and to M6 where the inhibitor is longer (at the top). But the vorticity strength is weaker with the 3D shape, in the PVS vortices as well as in the OVS vortices. Moreover, the vorticity field is a bit more perturbed. Some structures (more easily detectable with the criterion mergulian Q=0) can be suspected to stem from neighbouring locations of the inhibitor.

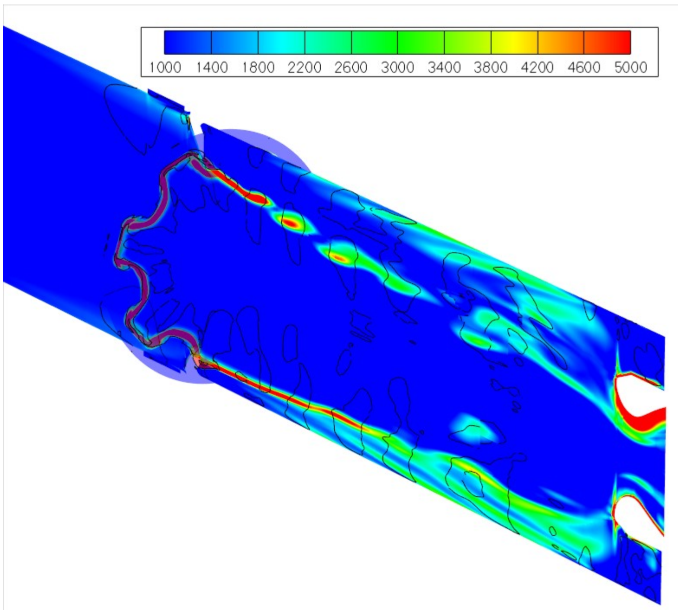

Illustration 8: Vorticity field, grid M4. Black lines : Iso-Q=0.

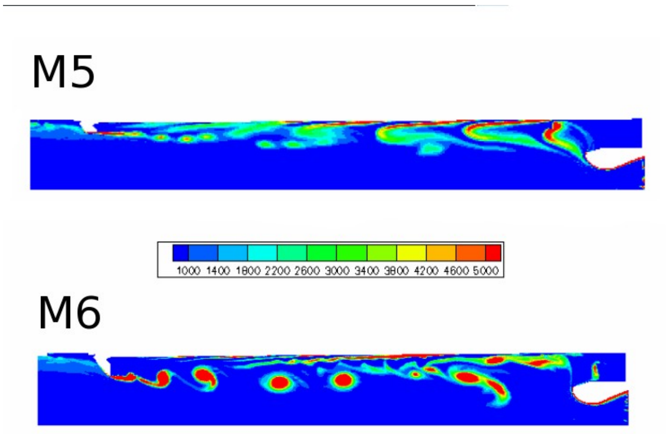

Illustration 9: Vorticity field, grids M5 and M6.

The plot of the fluctuating energy (figure 10) shows that it is stronger in the wake of the inhibitor and when the inhibitor is shorter. It can be due to the fact that the interaction of OVS and PVS is stronger and also to the orthoradial interaction of OVS vortices in this zone.
The computed instability levels with grids M5 and M6 were quite weak, close to the experiment. But these computations also showed that the interaction of OVS and PVS was different according to the inhibitor length. As a consequence, differences in the frequency spectra were obtained. The most excited longitudinal acoustic mode is the first one (1L) if the inhibitor is short. It seems to be due to a strong interaction of both hydrodynamic instabilities, OVS and PVS. With the longer inhibitor, a larger number of frequencies appear in the spectrum and the second longitudinal acoustic mode (2L) is strong. In this case, it appears that obstacle and parietal vortex sheddings are more independent. To allow a more relevant comparison, a 3D computation with a ring-shaped protruding inhibitor and a grid size around 4 million cells (as for grid M4) is being performed.

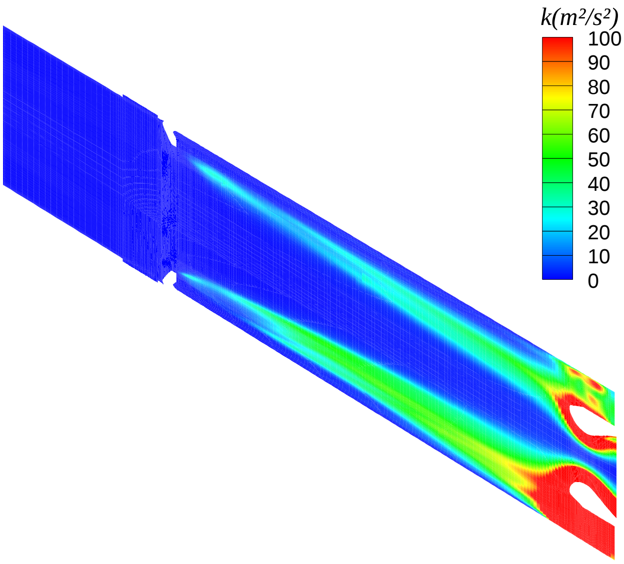

Illustration 10: Fluctuating energy $k=(u'^2+v'^2+w'^2)/2$.

COMPARISON BETWEEN EXPERIMENTAL AND NUMERICAL RESULTS

As sumed up in table 3, comparison to the experiment shows that the instability level is too low with grid M4. The mesh still needs to be refined.

Name	Frequency (Hz)	P_{rms} (Pa)
Experiment	568 ∓ 8	2,900
M0	/	/
M1	/	/
M2	/	/
M3	/	/
M4	244 ∓ 12.0	425
M5	312 ∓ 4.8	1,926
M6	297 ∓ 4.8	1,869

Table 3 Values at the head-end with different grids, compared to the experiment.

However, a zoom around time 8.6s in the HRogram analysis is shown in figure 11. It shows that similarly to what is observed in the computation (figure 7), the fluctuating energy around the first longitudinal acoustic mode is distributed over several peaks. Moreover, another major instability is locked on the second longitudinal acoustic mode (2L). It is even the main peak in the experiment whereas there is a little more energy around 1L mode in the computation. This little discrepancy also indicates that another refinement is still necessary but the spectral behaviour is globally satisfactory.

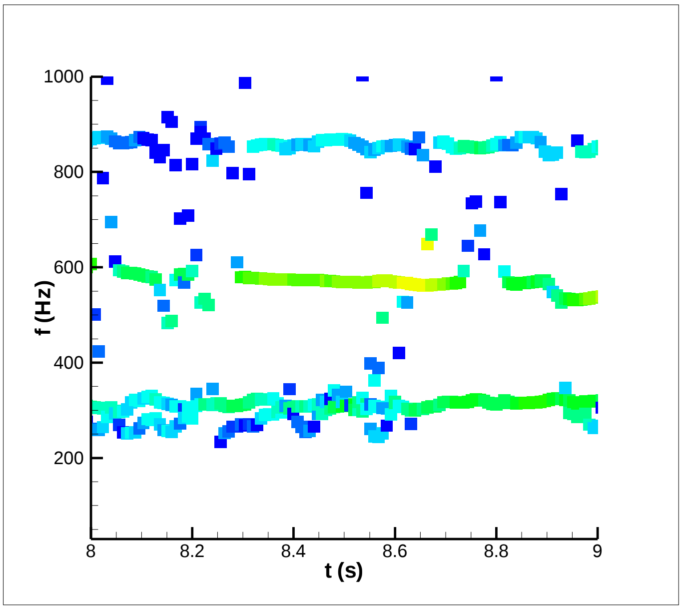

Illustration 11: HRogram analysis of pressure at the head-end, zoom around time 8.6s.

CONCLUSION

The influence of a 3D protruding inhibitor in a reduced-scale solid rocket motor was studied by numerical simulations. Several computations with different grid size were carried out in order to obtain some pressure oscillations. The instability level is low, still lower than in the experiment. But the spectral behaviour is quite satisfactory. A strong second longitudinal acoustic mode (2L) is found as well as some frequencies around the first longitudinal acoustic mode (1L).
Two types of vortex sheddings exist together in the chamber : parietal (PVS) and obstacle (OVS) vortex sheddings. Their strong interaction would lead to a reinforced PVS, and an instability locked on the 1L mode. The inhibitor being too high at its maximal height, this phenomenon is perturbed and a 2L mode appears. Moreover, it seems that the OVS vortices stemming from different heights of the inhibitor are in interaction, which is likely to enhance turbulence intensity.

ACKNOWLEDGEMENTS

The authors wish to thank Tristan Soubrié and Guillaume Turpin from ANDHEO for their contribution to the meshing, and the French space agency Centre National d'Etudes Spatiales (CNES) for supporting the test facilities and part of the simulations exposed in this paper.

REFERENCES

[1] M. Telara, L. Jacques, P. Le Helley, T. Pevergne, D. Ribereau, "A new concept to reduce SRM pressure oscillations: the 3D frontal thermal protection", European Conference in Aerospace Sciences (EUCASS) Moscow, 2005.
[2] J.-C. Traineau, M. Prévost, F. Vuillot, P. Le Breton, J. Cuny, N. Preioni, R. Bec, "A subscale test program to assess the vortex shedding driven instabilities in segmented solid rocket motors", 33rd AIAA/ASME/SAE/ASEE Joint propulsion conference & exhibit, 1997.
[3] R. Badeau, "Méthodes à haute résolution pour l'estimation et le suivi de sinusoïdes modulées. Application aux signaux de musique", PhD thesis, Ecole Nationale Supérieure des Télécommunications, 2005.
[4] R. Badeau, "Fast sequential ls estimation for sinusoidal modeling and decomposition of audio signals", 2007 IEEE Workshop on Applications of Signal Processing to Audio and Acoustics, 2005.